Numerical Simulations of Sheared Conditionally Unstable Flows over a Mountain Ridge

MARIO MARCELLO MIGLIETTA
ISAC-CNR, Lecce, Italy

RICHARD ROTUNNO
NCAR, Boulder, Colorado*

(Manuscript received 20 September 2013, in final form 6 January 2014)

ABSTRACT

In two recent papers, the authors performed numerical simulations with a three-dimensional, explicitly cloud-resolving model for a uniform wind flowing past a bell-shaped ridge and using an idealized unstable (Weisman–Klemp) sounding with prescribed values of the relevant parameters. More recently, some observed cases of orographically forced wind profiles were analyzed, showing that, in order to reproduce larger rainfall rates, it was necessary to initialize the sounding with low-level flow toward the mountain with weak flow aloft (as observed). Additional experiments using the Weisman–Klemp sounding, but with nonuniform wind profiles, are performed here to identify the conditions in which the presence of a low-level cross-mountain flow together with calm flow aloft may increase the rain rates in conditionally unstable flows over the orography. The sensitivity of the solutions to the wind speed at the bottom and the top of a shear layer and the effect of different mountain widths and heights are systematically analyzed herein.

Large rainfall rates are obtained when the cold pool, caused by the evaporative cooling of rain from precipitating convective clouds, remains quasi stationary upstream of the mountain peak. This condition occurs when the cold-pool propagation is approximately countered by the environmental wind. The large precipitation amounts can be attributed to weak upper-level flow, which favors stronger updrafts and upright convective cells, and to the ground-relative stationarity of the cells. This solution feature is produced with ambient wind shear within a narrow region of the parameter space explored here and does not occur in the numerical solutions obtained in the authors' previous studies with uniform wind profiles.

1. Introduction

Orographic convection is the result of processes active in a moist, conditionally unstable troposphere on a range of different space and time scales including synoptic forcing, mesoscale orographic uplift, and the microphysics of clouds and rain (Sawyer 1956). The variety of terrain scales, heights, and orographic shapes, the nonstationarity of real atmospheric conditions and airflow, and the nonlinearity of the interaction between topographic disturbances and synoptic systems require investigation from both a modeling and observational perspective. Thus, a variety of dedicated terrain-related field observation programs has been undertaken in the last few years in different parts of the world, including the Southwest Monsoon Experiment/Terrain-Influenced Monsoon Rainfall Experiment (SoWMEX/TiMREX; Davis and Lee 2012), the Mesoscale Alpine Programme (MAP; Rotunno and Houze 2007) and the MAP Demonstration of Probabilistic Hydrological and Atmospheric Simulation of Flood Events (MAP-DPHASE; Rotach et al. 2009) projects, and the Convective and Orographically-Induced Precipitation Study (COPS; Wulfmeyer et al. 2011).

Orographically influenced, heavy-rain convective events are well documented in the literature all over the world [see Richard et al. (2007) for a review]. Although the timing, evolution, and location can differ greatly from case to case, some common ingredients have been

* The National Center for Atmospheric Research is sponsored by the National Science Foundation.

Corresponding author address: Mario Marcello Miglietta, CNR-ISAC, Strada Provinciale Lecce-Monteroni, 73100 Lecce, Italy.
E-mail: m.miglietta@isac.cnr.it

DOI: 10.1175/JAS-D-13-0297.1

identified at both the mesoscale and synoptic scale—for example, an upper-level short-wave trough combined with a region of conditionally unstable air, and weak middle- and upper-tropospheric currents (Pontrelli et al. 1999; Lin et al. 2001). The presence of an intense low-level, moist airflow impinging on the mountain is also a frequently observed feature, as it provides an adequate supply of moisture and focuses deep convection over the same area for several hours (Buzzi and Foschini 2000; Nuissier et al. 2008; Ducrocq et al. 2008). These processes, which were the focus of the California Land-Falling Jets Experiment (CALJET) and Pacific Land-Falling Jets Experiment (PACJET) projects (Neiman et al. 2005), represent an effective mechanism for triggering and maintaining convection by producing the uplift of the air parcels near the ground; such forcing can be sufficient to remove convective inhibition and initiate convection (e.g., Smith 1979; Buzzi and Foschini 2000; Bousquet and Smull 2003).

Because of the short life cycle of single convective cells, large rainfall amounts are generally expected to occur when different cells are repeatedly triggered in a limited region for several hours and continually precipitate approximately in the same location, often producing flash flooding. The complex nature of the terrain may result in localized areas of persistent convergence that repeatedly triggers convection over the same locations (Kodama and Barnes 1997). However, cells, after formation, may move according to the wind aloft and thus produce rain at another location, or, rather, a cold outflow may trigger cells far from the mountain. In such cases, convectively induced cold pools and outflows can be very important in either allowing the propagation of convective systems or focusing, together with the orography, convective cell development in a confined area (Senesi et al. 1996; Romero et al. 2000).

From a theoretical point of view, it is difficult to determine the conditions favorable for heavy precipitation at a precise location. Numerical idealized studies of orographic deep convection are relatively few and challenging, mainly because of the large number of mesoscale factors (i.e., properties of the upstream wind and temperature profiles, the shape of the mountain, etc.) involving the complex nature of moist convection (e.g., Yoshizaki and Ogura 1988), the three-dimensional stochastic nature of turbulent convection interacting with precipitation (Bryan et al. 2003), and the complexity of the microphysics processes related with the production of precipitation (Rotunno and Houze 2007).

In two recent papers (Miglietta and Rotunno 2009, hereafter MR09, and Miglietta and Rotunno 2010, hereafter MR10), the authors reported on numerical simulations of conditionally unstable flows over an idealized mesoscale mountain ridge. The numerical solutions were carried out for a uniform wind and using an idealized unstable sounding with prescribed values of the relevant parameters. Different experiments were undertaken by changing the environmental wind speed U, the mountain half-width a and height h_m, and sounding parameters [e.g., the level of free convection (LFC), the convective available potential energy (CAPE)], thus allowing for the investigation of simulated precipitation characteristics as a function of the prescribed environment. Analyzing numerous simulations, they were able to identify different flow regimes, classified according to the values of three different nondimensional numbers: the mountain slope h_m/a, controlling the organization of the orographic rainfall; the ratio between an advective time scale $\tau_a = a/U$ and a convective time scale $\tau_c = h_t/(\mathrm{CAPE})^{1/2}$ (where h_t is the tropopause height); and the ratio of the mountain height to the level of free convection (h_m/LFC), controlling the triggering of convection (no rainfall was obtained for the case of short mountains). For weak wind speed and/or large instability (i.e., $\tau_a/\tau_c \gg 10$), the solution was dominated by rapidly propagating cold pools induced by the evaporation of rainfall and thus there were no stationary solutions of intense rainfall near the mountain; thus, quasi-stationary solutions could be obtained only in a very narrow region of the parameter space (h_m/a, h_m/LFC, τ_a/τ_c).

A special solution occurs for the case of low CAPE (MR10): in this circumstance, the rainfall amount and the characteristics of the solution are fairly independent of the three parameters identified above. Thus, two additional parameters—$(\mathrm{DCAPE})^{1/2}/U$ (where DCAPE is the downdraft CAPE) and $N(\mathrm{LFC}/U)$ (where N is the Brunt–Väisälä frequency)—needed to be considered, related respectively to the cold-pool propagation speed and to the deceleration induced by the cold pool on the upstream flow.

More recently, the application of the theoretical results of these two papers to observed cases of orographically forced convective rainfall—including the Big Thompson Flood (1976, Colorado), the Oahu Flood (1974, Hawaii), and the Gard Flood (2002, France)—was analyzed (Miglietta and Rotunno 2012, hereafter MR12). Specifically, numerical simulations were carried out using idealized soundings relevant to these cases. Although the real meteorological situation was nonstationary and spatially varying, and the real topography was three dimensional, the simulations produced solutions qualitatively consistent with the observations and with those expected from the theory developed in MR09 and MR10, as simulated rain rates fit reasonably well within the previous theoretically derived parameter space. Thus, the theory developed in MR09 and MR10 can be, at least qualitatively, applied to soundings different from the prototypical Weisman–Klemp profile.

However, in order to reproduce larger rainfall rates, in closer quantitative agreement with observations, in the former two cases it was necessary to initialize the model with a wind profile more consistent with the observations, characterized by low-level flow toward the mountain with stagnant region aloft (only the component perpendicular to the ridge was considered). The inclusion of this vertical wind shear was effective in almost doubling the rainfall rates with respect to the case with uniform environmental wind. For a third case, the inclusion of a low-level flow with weak wind aloft did not significantly modify the rainfall amount and distribution. Also, the choice of an appropriate initial sounding emerged as fundamental in order to reproduce the characteristics of the observed rainfall pattern and evolution (Davolio et al. 2009).

To generalize these results, the present paper systematically analyzes the sensitivity of the rainfall-rate maximum and its location to changes in the vertical wind profiles. Additional experiments using the Weisman and Klemp (1982) sounding (with initial values of CAPE of approximately 1480 J kg^{-1} for a surface parcel, 2300 J kg^{-1} for the most unstable parcel,[1] DCAPE $\sim$ 880 J kg^{-1}, LFC $\sim$ 1800 m), but with nonuniform wind profiles, are performed in order to ascertain if the presence of a strong low-level cross-mountain flow together with calm flow aloft may increase the rainfall rates in conditionally unstable conditions and the region of the parameter space where this may occur. The sensitivity of the solutions to the wind speed at the bottom and the top of the shear layer and to the height and depth of the shear layer are systematically analyzed for different mountains.

It is known that vertical wind shear, in the absence of orography, is effective in producing high rainfall rates in mesoscale convective systems (Rotunno et al. 1988). For example, a squall line in the presence of low-level shear produces, compared to the cases with constant wind, deeper and more intense updrafts, stronger cold pools, and locally heavier precipitation, as described in Rotunno et al. (1988), Weisman and Rotunno (2004), and Bryan et al. (2006). However, only a few studies considered the role of wind shear in orographic convection, from both an observational and a numerical perspective. Houze and Medina (2005) found that a layer of strong shear at the top of a low-level layer of apparently retarded or blocked flow (as shown by Doppler radial velocity data) provided a favorable environment for the turbulent cells to develop. Kirshbaum and Durran (2005a), Miniscloux et al. (2001), and Yoshizaki et al. (2000) proposed that the low-level wind shear plays an important role in the organization of the orographic rainbands associated with shallow convection; this result was later supported by idealized numerical simulations (Kirshbaum and Durran 2005b; Fuhrer and Schär 2007). However none of these studies considered the influence of vertical wind shear on deep orographic convection in a systematic way. Since the wind shear and the orography are, separately, favorable factors for increasing the rainfall amount, it will be explored here if the combination of the two factors also has a positive effect on the orographic precipitation amount.

The paper is organized as follows. In section 2, the numerical setup is described, and the parameters relevant for the present study are presented. The results of the numerical experiments are described and analyzed in sections 3 and 4, respectively, for the simulations with and without a mountain. Additional experiments, including changes in the shear-layer extent and depth, and changes in the mountain shape, are analyzed in section 5. Discussion and concluding remarks are given in section 6.

2. Numerical setup

As in the previous papers by the authors (MR09; MR10; MR12), the present idealized simulations are performed with a three-dimensional, cloud-resolving model (Bryan and Fritsch 2002). Compared to the previous work, a newer model version is used (release 16 instead of 8). The main improvement in this version is a correction in the calculation of the gradients in the proximity of the orography when vertically stretched grids are used, as in the present study. As in the previous papers, simulations are performed for 10 h—a time long enough to identify the statistically stationary (along-ridge averaged) features of the solution precipitation characteristics. In the following figures, instantaneous fields will be shown at that time.

The numerical setup is similar to that described in MR09, with 59 stretched vertical levels, having a vertical spacing of 250 m below 9000 m and 500 m above 10 500 m. The mountain peak is located 20 km downstream of the domain center, and random noise is added to the topography (see MR09 for details). The extent of the along-mountain domain length is 20 km, with a horizontal grid spacing of 250 m. [Preliminary experiments using a two-dimensional setup show some differences with respect to their three-dimensional counterparts; in particular, the cold pool is too intense in the former case,

[1] Note that the values of CAPE slightly differ from those in MR09 and MR10, as a more accurate program for the calculation of CAPE is now used.

thus suggesting the need for a fully three-dimensional simulation to reproduce the essential physics (see also Fuhrer and Schär 2005).]

In contrast with MR09, grid stretching is also applied in the cross-mountain horizontal direction in order to extend the domain and keep the open boundaries farther from the mountain. The inner part of the domain is similar to that used in MR09, having 1280 points with horizontal grid spacing of 250 m. The grid spacing gradually increases to 1250 m in the outer 320 points (160 points on each side), for a total of 1600 grid points and a length of 560 km. Compared to MR09, the microphysics is also changed as the double-moment Morrison scheme is now used, with a cloud droplet concentration of 200 cm^{-3}, which is intermediate between maritime and continental environments. The adaptive-time-step option is active so that the model automatically adjusts the time step to maintain numerical stability. In the present study, the effect of the Coriolis force is neglected, although its inclusion may significantly affect the cold-pool dynamics (through geostrophic adjustment), limiting the horizontal scale of the circulation, thus reducing the upstream cold-pool propagation and producing a decay in the storm intensity (Fovell 1991; Szeto and Cho 1994). The east–west (perpendicular to the mountain ridge) boundaries are open, while the north–south (along mountain) boundaries are periodic. The near-surface boundary layer and radiation physical processes are switched off in the model integration.

In the initial set of experiments, the mountain, whose profile is a "witch of Agnesi," has been kept constant (h_m = 2000 m, a = 30 km) as well as the sounding, which is the Weisman and Klemp (1982) profile—a prototype for convectively unstable conditions. Note that, since there is latent heating (and thus reduced static stability), flow blocking is not expected for such a mountain.[2] To test the sensitivity of the solution to wind variation with height, the following parameters have been changed: the wind speed at the bottom U_s and at the top U_∞ of a shear layer, and the depth of the shear layer h_s, where the wind speed changes linearly from U_s to U_∞. In this initial set of experiments, the shear layer starts from the surface; however, the experiments in MR12 were initialized with a profile of constant wind speed in a layer near the ground (1 km deep for Big Thompson, about 3 km for Oahu and Gard cases). For this reason, the height Z_s of the layer with constant wind has also been varied in an additional set of experiments. All the parameters that are varied in the present study are shown in Fig. 1.

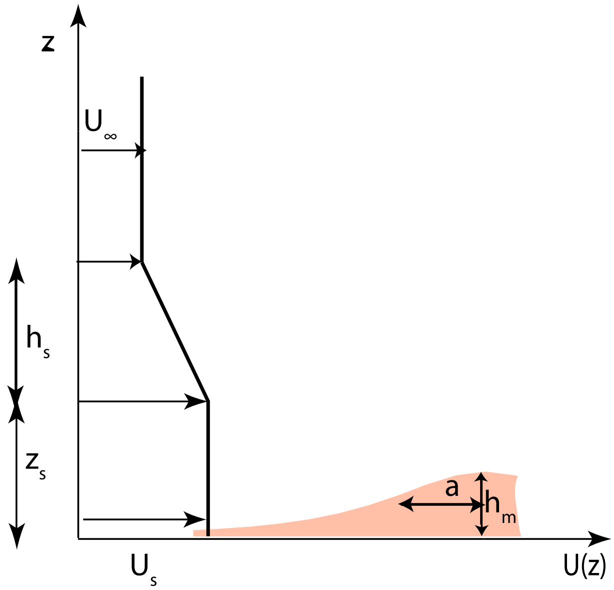

FIG. 1. Parameters varied in the experiments.

3. Experiments with mountains

The initial experiments are performed varying U_s and U_∞, with h_s = 5 km and Z_s =0. The full list of this set of experiments is shown in Table 1. The metrics used herein to measure rainfall intensity are defined as follows. The rain rate at the surface $z = h(x, y)$ is defined as $R(x, y, t) = (V_T\rho_r)_{z=h(x,y)}$, where V_T is the terminal velocity of raindrops (m s^{-1}) and ρ_r is the rainwater amount per cubic meter of air (kg m^{-3}). The units of R therefore are kilograms per square meter per second. Since liquid water has a density of 1000 kg m^{-3}, by convention the units kilograms per square meter in R are replaced by millimeters to indicate that the rain rate is measured by the amount of rain necessary to fill a 1-m^2 column by 1 mm. As a measure of rainfall intensity the along-ridge, hourly average rain rate

$$\overline{R}(x,t_i) = \frac{1}{h}\int_{t=t_{i-1}}^{t_i}\left[\frac{1}{l_y}\int_{y=0}^{l_y} R(x,y,t)\,dy\right]dt, \qquad (1)$$

where $t_i = i \times 1h$ and l_y is the domain length in the along-ridge direction is considered. For the nearly stationary patterns of rainfall near the ridge, it is convenient to define a maximum rain rate as the

$$R_{\max} = \frac{1}{3}\max_{0\le x\le l_x}\sum_{i=7}^{10}\overline{R}(x,t_i), \qquad (2)$$

[2] Additional simulations, which have been performed removing all latent cooling, show that flow blocking is not present in these solutions, and thus it does not affect the cold-pool propagation.

TABLE 1. List of experiments with $h_s = 5$ km and $Z_s = 0$ ($h_m = 2000$ m, $a = 30$ km; $h_m/a = 0.07$; h_m/LFC = 1.11) and varying input values of U_s and U_∞ (m s^{-1}). Nonstationary solutions are indicated by "NS." The location of the maximum rain rate X_{max} relative to the mountain ridge top is given in km; τ_a/τ_c is calculated considering the average wind speed in the lower 5 km.

Expt	U_s (m s^{-1})	U_∞ (m s^{-1})	R_{tot} (10^3 mm h^{-1} km^2)	R_{max} (mm h^{-1})	X_{max} (km)	τ_a/τ_c	Figures
A.1	5	0.0	14	NS		46.2	
A.2	5	5.0	10	NS		23.1	
A.3	10	0.0	21	NS		23.1	Figs. 3a,b
A.4	10	5.0	12	6	−50	15.4	
A.5	10	5.5	12	8	−25	14.9	
A.6	10	6.0	12	6	−7	14.4	
A.7	10	7.0	11	6	−6	13.6	
A.8	10	10.0	9	6	−5	11.5	Figs. 2a,b
A.9	15	0.0	23	NS		15.4	
A.10	15	3.0	19	24	−10	12.8	
A.11	15	5.0	16	9	−9	11.5	
A.12	15	10.0	13	9	−4	9.2	
A.13	15	15.0	11	10	−4	7.7	
A.14	20	0.0	28	30	−42	11.5	Figs. 3c,d
A.15	20	1.0	26	22	16	11.0	
A.16	20	5.0	20	13	−4	9.2	
A.17	20	10.0	16	14	−5	7.7	
A.18	20	20.0	15	16	−1	5.8	Figs. 2c,d
A.19	20.5	0.5	26	31	−9	11.0	
A.20	21	1.0	28	27	20	10.5	
A.21	23	3.0	23	14	−10	8.9	
A.22	25	−2.0	36	32	−9	10.0	
A.23	25	0.0	31	31	30	9.2	
A.24	25	5.0	24	16	−10	7.7	
A.25	25	25.0	16	21	7	4.6	

where l_x is the domain length in the across-ridge direction; the position $x = X_{max}$ is the location of R_{max}. Finally, the area-total hourly rain rate is defined as

$$R_{tot} = \frac{1}{10h}\int_{t=0}^{10h}\int_{y=0}^{l_y}\int_{x=0}^{l_x} R(x,y,t)\,dx\,dy\,dt. \quad (3)$$

To provide a reference point for the present simulations with orography, simulations without a mountain have also been done; in this case the simulations are typical of squall-line studies, except here the environmental wind profiles will be set in order to compare certain solution features with and without mountains. Given that most of the parameter space will be characterized by a moving convective systems, a modified form of (2),

$$R^*_{max} = \frac{1}{3}\sum_{i=7}^{10} \max_{0\le x\le l_y} \overline{R}(x,t_i), \quad (4)$$

is used in an attempt to track the generally moving maximum; $R^*_{max} \approx R_{max}$ for nearly stationary systems.

First, results are shown for the cases with uniform wind speed. Figure 2 shows the Hovmöller diagram of $\overline{R}(x, t_i)$ (Figs. 2a,c) and the vertical cross section of the y-averaged potential temperature perturbation Θ' (negative values only), rainwater, cloud water, and ice content (Figs. 2b,d) for the cases (U_s, U_∞) = (10, 10) (expt A.8) and (U_s, U_∞) = (20, 20) m s^{-1} (expt A.18). As shown in MR09, in both cases a stationary solution occurs, which is characterized by R_{max} located just upstream of the mountain (see X_{max} in Table 1). However, for the case U_s = 10 m s^{-1}, a secondary maximum occurs downstream (Fig. 2a), generated by the convergence between the cold pool produced by rainfall evaporation near the ground and the leeside orographic downslope flow (cf. Fig. 2b with MR09's Fig. 5b).

Next, wind shear is added to the initial condition: two simulations are analyzed, sharing the same value of U_s as the previous two experiments, but with U_∞ reduced to 0. For U_s = 10 m s^{-1} (expt A.3, Fig. 3a), no stationary rain is simulated close to the mountain, since the cold pool propagates upstream as a density current toward the entrance of the channel (Figs. 3a,b), similar to the solutions with weak wind in MR09 (their Fig. 5a). Apparently, compared with the case with uniform wind profile U_s = U_∞ = 10 m s^{-1} (Figs. 2a,b), here the reduced vertically averaged wind speed allows the cold pool to propagate upstream rather than remaining near the mountain peak (on the downstream side).

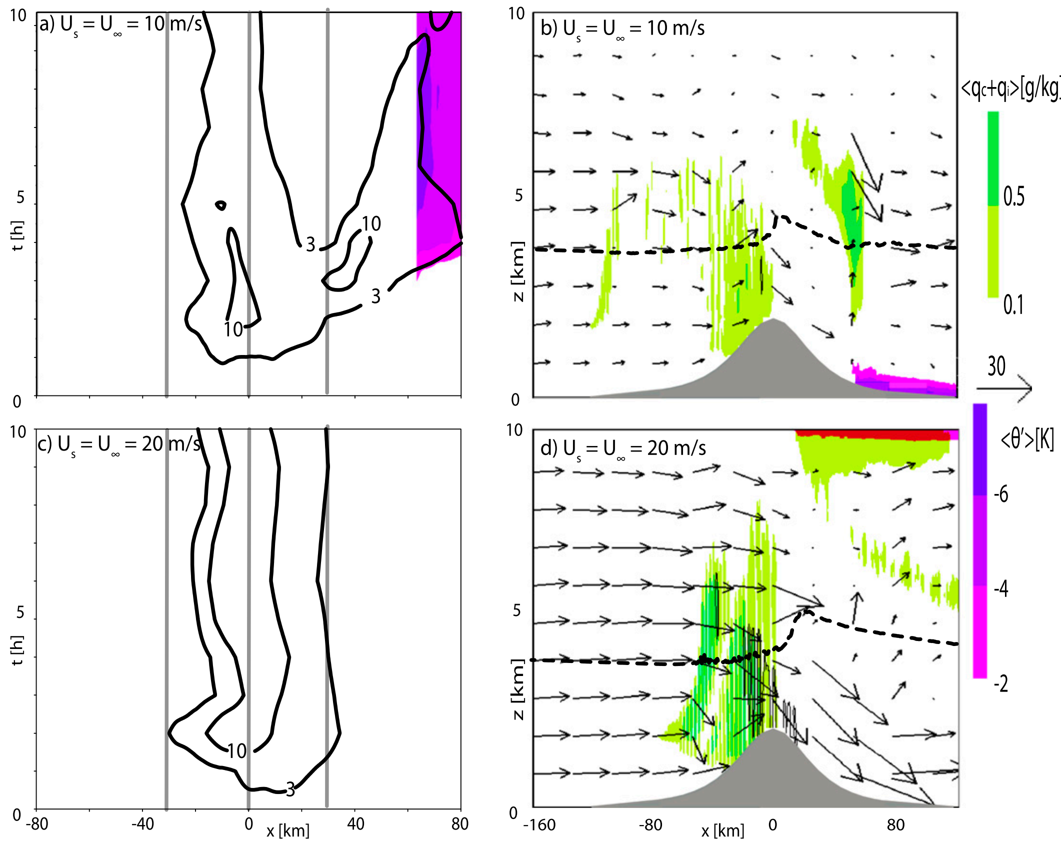

FIG. 2. Uniform wind cases: (a),(c) Hovmöller diagram of $\overline{R}(x, t_i)$ from (1) (mm h^{-1}) and of the y average of potential temperature perturbation (K, purple shaded areas) at the second model level (z = 375 m); (b),(d) vertical cross section of the y average of potential temperature perturbation (K, purple shaded areas), cloud water plus ice content (g kg^{-1}, green shaded areas), rainwater content (solid contour line for 0.5 g kg^{-1}), wind vectors (arrows), and 0°C isotherm (dashed line). The results are shown for (top) expt A.8 ($U_s = U_\infty = 10$ m s^{-1}) and (bottom) expt A.18 ($U_s = U_\infty = 20$ m s^{-1}). The vertical cross sections are shown at the final integration time, t = 10 h. $\overline{R}(x, t_i)$ is calculated every 1 h from t = 0 to 10 h. The vertical gray lines represent the locations of the ridge top and half-width distances.

For $(U_s, U_\infty) = (20, 0)$ m s^{-1} (expt A.14, Fig. 3c), very large values of $\overline{R}(x, t_i)$ are obtained. This solution, which shows a deep cold pool propagating very slowly upwind, is located just upstream of the mountain (Fig. 3d) and has no counterpart in the constant-ambient-wind results in MR09.[3] The solutions in Fig. 3 have different characteristics compared to both cases with uniform wind speed shown in Fig. 2, with which they share, respectively, the surface wind (expt A.18) and the wind speed average in the lowest 5 km (expt A.8). These considerations suggest that the character of this solution is the result of the inclusion of shear in the wind speed profile.

Figure 4 shows in a two-dimensional graph R_{max} (Fig. 4a) and X_{max} (Fig. 4b) for different values of U_∞ and U_s. Heavy-rain quasi-stationary solutions, similar to that shown in Fig. 3d, occur within a narrow region of the parameter space, around a thick dashed line separating the two main categories of solutions, characterized, respectively, by "orographic rainfall" (such as those in Fig. 2) and "nonstationary cold pool" (as in Figs. 3a,b). The separation line intersects $U_\infty = 0$ for values of U_s between 20 and 25 m s^{-1}; that is, the heavy-rain solutions require negative values of U_∞ for larger U_s (as in expt A.22).

For values of U_∞ above the separation line (thick dashed line in Fig. 4), the wind speed is sufficient to arrest the upstream cold-pool propagation, and statistically stationary convective cells are triggered by the mountain, with R_{max} values similar to those in the cases with uniform wind speed (thin, solid diagonal line in

[3] In MR10, a balance between the density current and the environmental flow was simulated for low values of CAPE. However, the solution produced relatively low rainfall rates and was associated with very specific environmental conditions.

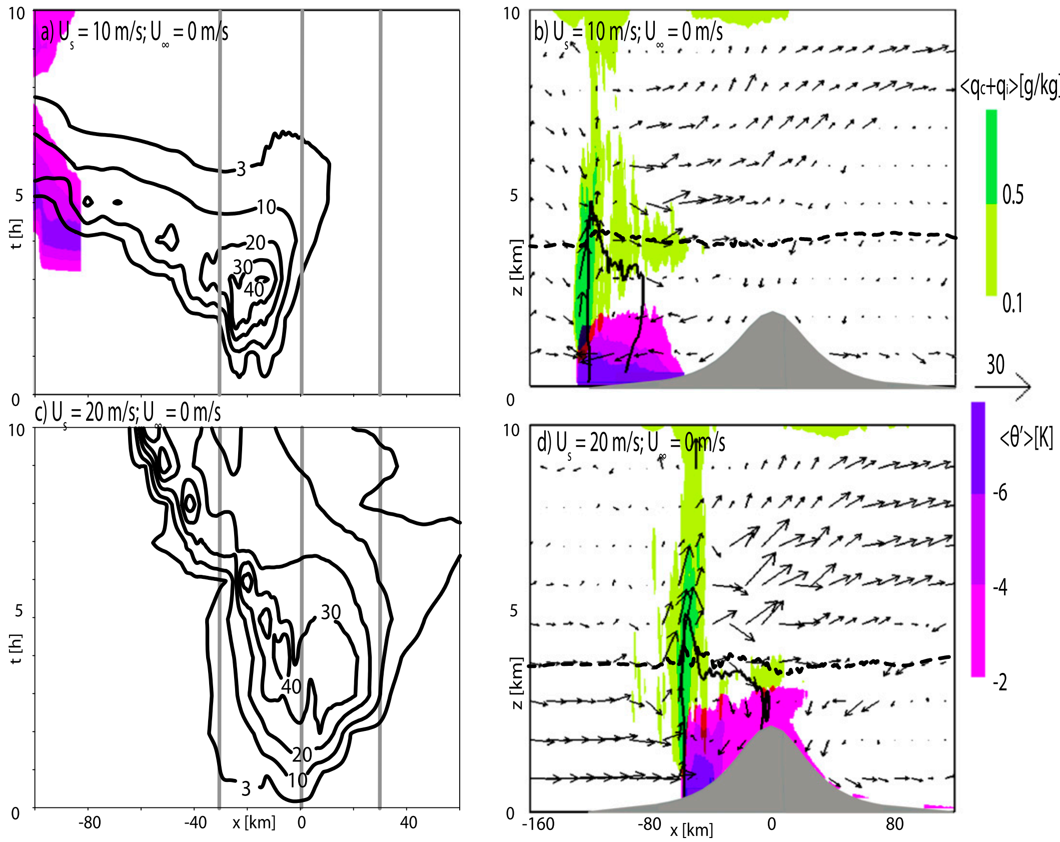

FIG. 3. Zero-wind-aloft cases: as in Fig. 2, but for (a),(b) expt A.3 ($U_s = 10\,\mathrm{m\,s^{-1}}$, $U_\infty = 0\,\mathrm{m\,s^{-1}}$) and (c),(d) expt A.14 ($U_s = 20\,\mathrm{m\,s^{-1}}$, $U_\infty = 0\,\mathrm{m\,s^{-1}}$). The vertical cross sections are shown, respectively, at $t = 6$ h (expt A.3) and at the final integration time $t = 10$ h (expt A.14).

Fig. 4); thus, the shear has almost no effect on the rainfall in this region of the parameter space. The $R_{\max}$ location ($X_{\max}$) is generally upstream, except for the case of very large U_s, in which $R_{\max}$ may be slightly downstream (upper-right side in Fig. 4b). On the other hand, for values of U_∞ below the thick dashed line, the vertically averaged wind speed is too weak and cannot prevent the cold pool from propagating far upstream from the obstacle; thus, no stationary solution is obtained in this case. As a consequence, the rainfall distribution shifts far upstream (Fig. 4b).

It is apparent from Fig. 4 that the region of the parameter space around the separation line is sensitive to small variations in wind speed, as a change of $1\,\mathrm{m\,s^{-1}}$ in U_∞ for a given value of U_s can produce a significant change in solution characteristics. The slope of the separation line, which forms an angle of about 30° with the abscissa, suggests a stronger dependence on U_∞ than on U_s. The quantity $R_{\max}$ exhibits a very strong gradient on either side of this line; in particular, the $R_{\max}$ values are twice as large as those simulated in the case of stationary orographic rainfall for the same value of U_s. A similar increase is also noted for R_{tot} (Table 1). The increased rainfall in these solutions is due to a subtle balance, occurring when the cold-pool propagation upstream is approximately countered by the environmental wind. As a consequence, the cold pool is quasi stationary and remains confined immediately upstream of the mountain peak (Fig. 4b). In this way, the uplift induced by the cold pool reinforces the orographic forcing, producing deep and quasi-stationary convective cells.

The foregoing considerations also apply to the region just below the thick dashed line, where the cold pool still remains nearly stationary upstream, as in the case (U_s, U_∞) = (20, 0) $\mathrm{m\,s^{-1}}$ (expt A.14), for which the propagation speed is only approximately $-3\,\mathrm{m\,s^{-1}}$. In the region just above the dashed line, an approximately stationary rainfall pattern still occurs, but $R_{\max}$ is located downstream. For example, in expt A.15 [(U_s, U_∞) = (20, 1) $\mathrm{m\,s^{-1}}$], the density current head remains quasi stationary on the downwind side of the mountain ridge (Figs. 5c,d), in a location characterized by downward mountain-induced motion; thus, the uplift induced by cold pool is somewhat countered. The $R_{\max}$ value in this

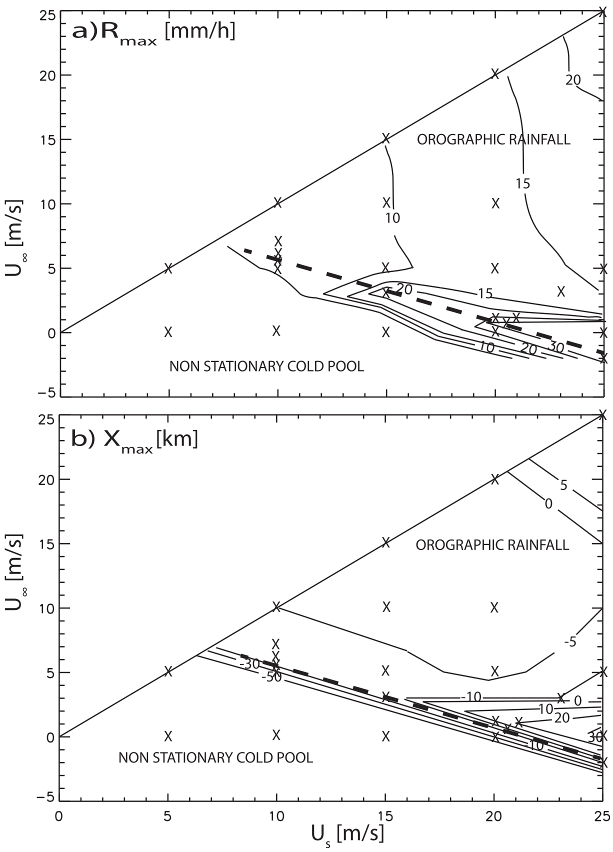

FIG. 4. (a) R_{max} from (2) ($mm\,h^{-1}$) and (b) X_{max} (km) of the y-averaged rain-rate peak as a function of U_s and U_∞ ($m\,s^{-1}$); the crosses correspond to the experiments. The thick dashed line represents the region corresponding to heavy-rain quasi-stationary solutions, and separates the two main categories of solutions (i.e., orographic rainfall and nonstationary cold pool).

case, although larger than for the orographic stationary solution, is much smaller than in exp. A.19 [$(U_s, U_\infty) = (20.5, 0.5)\,m\,s^{-1}$], since the cold pool in exp. A.15 [$(U_s, U_\infty) = (20, 1)\,m\,s^{-1}$] is located less favorably with respect to orographic lifting. The differences are remarkable considering that the two experiments differ only by a very small change in environmental wind speed (cf. Figs. 5a,b and 5c,d).

These results show that the reverse wind shear profiles analyzed in the present study have a positive effect on the rainfall amount compared to simulations with uniform wind, confirming the outcomes of MR12, and in particular of the Big Thompson case simulation, where similar control parameters were selected. Figure 6 summarizes these considerations for the simulations with $U_s = 10$ and $20\,m\,s^{-1}$, respectively in conditions of constant wind and of zero wind aloft.

Compared to the cases with shear, simulations without shear are characterized by shallower updrafts and weaker cold pools (Fig. 6). The hypothesis was explored that this behavior could be, at least in part, attributed to the different structure of the dry analytical solution in cases with and without the presence of a critical level. Starting from the analytical solutions for a Fourier component given in Klemp and Lilly (1975), solutions were calculated for the case of a bell-shaped mountain, through a Fourier composition, respectively, for the case with constant wind and for an atmosphere with linear shear and a critical level at 5 km. The comparison between the two solutions (not shown) indicates that for the case with a uniform wind, a region of positive buoyancy extends in the upper levels up to the tropopause on the upstream side of the mountain, thus making the atmosphere more stable and reducing the vertical extent of the region with CAPE (downward displacement and drying, which are associated with positive buoyancy, tend to further suppress convection). For the case with shear, the solution shows a slanted wave structure, with positive regions of buoyancy extending only to the critical level, thus favoring the presence of larger instability and deeper ascending motion in the upper troposphere.

However, the analysis of the numerical simulations indicates that the difference in upstream convective stability produced by the wave features associated with the presence of the shear have little explanatory power. The orographic precipitation characteristics of the solutions appear mainly as the result of the interaction between the environmental wind profile and the intensity of the cold pool, and that these linear-wave effects based on dry dynamics are at most minor factors. Without shear, the upper-level wind is stronger and causes the downstream advection of clouds, and there is less time for the cold pool to develop. On the other hand, in the presence of shear, if the lower-layer wind speed is sufficient to counter the propagation of the cold pool, cells produced by cold-pool lifting enter an upper layer with zero flow and thus do not move with respect to the mountains (this factor is usually mentioned in observational studies), and therefore they produce quasi-stationary rainfall.

In conclusion, the larger rainfall amount in the simulations with shear can be attributed mainly to the deeper updrafts of the convective cells and to their ground-relative stationarity. Additionally, the effect of the mountain barrier on the cold pool affects the precipitation distribution behaving as an extension of the orographic obstacle. This effect will be explored further below.

4. Experiments without mountains

In the present section, simulations without mountains are discussed for the sake of comparison with the

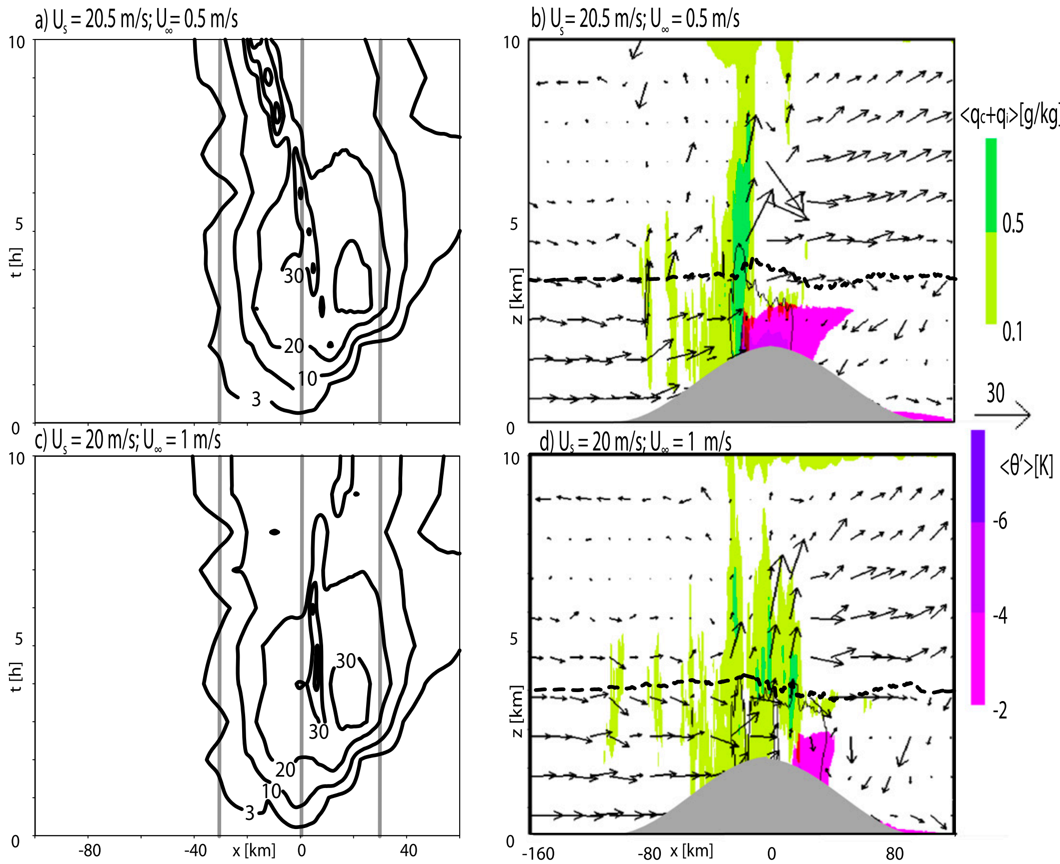

FIG. 5. As in Fig. 2, but for (a),(b) expt A.19 ($U_s = 20.5\,\mathrm{m\,s^{-1}}$, $U_\infty = 0.5\,\mathrm{m\,s^{-1}}$) and (c),(d) expt A.15 ($U_s = 20\,\mathrm{m\,s^{-1}}$, $U_\infty = 1\,\mathrm{m\,s^{-1}}$). The vertical cross sections are shown at the final integration time $t = 10\,\mathrm{h}$.

experiments described above. These simulations are implemented in a similar fashion to that described in Rotunno et al. (1988), Weisman and Rotunno (2004), and Bryan et al. (2006): the terrain is flat throughout the domain and a squall line is initialized with a −1.5-K perturbation in potential temperature θ' plus small random perturbations to trigger three-dimensional motion (temperature perturbations were initialized in different locations for each case to allow a longer residence time on the downshear side of the cold pool in the inner part of the domain). Since a horizontal grid spacing of 250 m is chosen here in the inner part of the domain (as in MR09, MR10, and MR12), the solutions cannot be compared exactly with these previous studies, where a coarser grid spacing and a different-sized domain were considered. Since the solutions are theoretically Galilean invariant, their features should be independent of the value of the vertically averaged environmental wind; thus, any difference for a fixed value of U_s should only be ascribed to the wind shear $U_s - U_\infty$. This is consistent with the results in Table 2, which shows that the total rainfall amount R_{tot} is mainly a function of wind shear: the discrepancy in R_{tot} among experiments with the same shear is very small, confined at most to within about 20% for the cases with large values of $U_s - U_\infty$.

For the set of experiments discussed in the present section, solutions with nearly stationary ground-relative propagation occur only within a narrow range of values of U_s and U_∞; thus, R_{max}, calculated by (2), is very small in most of the simulations, precluding the possibility of a comparison with the experiments in Table 1. For this reason, the rain rate is measured in this set of simulations by R^*_{max} in (4). Equation (4) is nearly equivalent to calculating the rain-rate peak in a reference frame following the convective system. However, since the model output is saved at time intervals of 1 h, the rainfall occurring in this period distributes rain over several grid points in the simulations where the cold pool propagates quickly, while the rainfall will accumulate in the same location in cases of quasi-stationary cold pools. As a consequence, in the former case R^*_{max} will be smaller as compared to the latter case, although the rain rate calculated in each time step would be the same. Thus, R^*_{max} cannot be used to infer the Galilean invariance of these experiments.

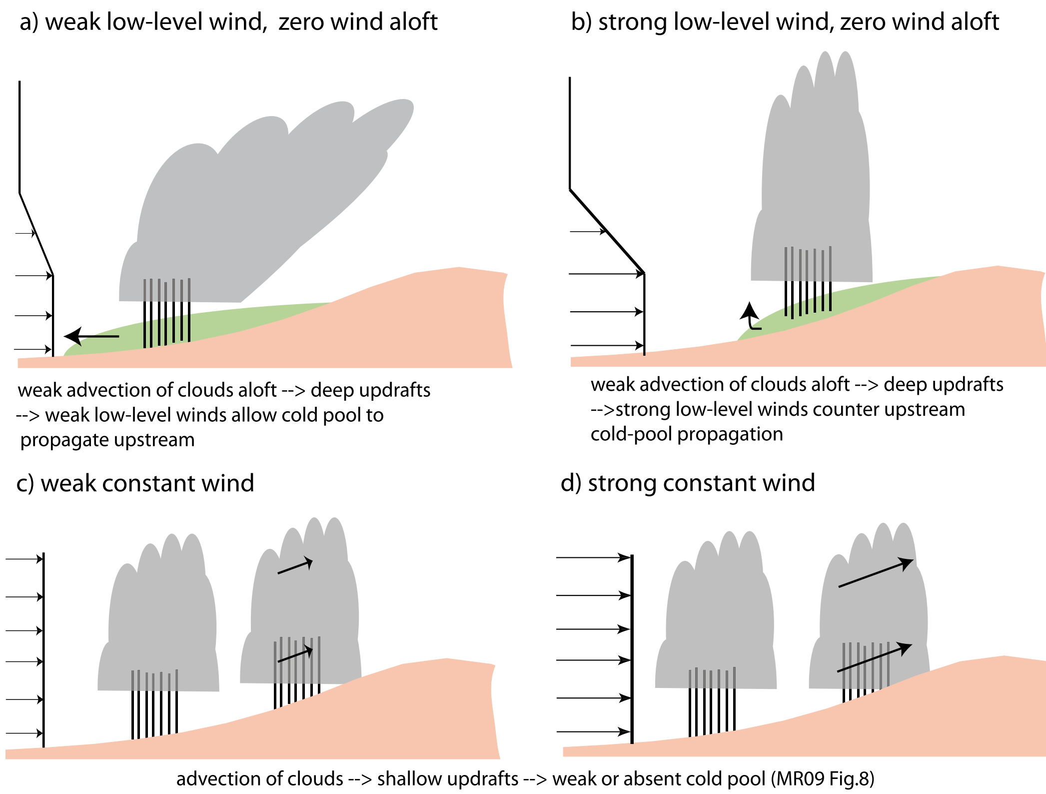

FIG. 6. Conceptual models for the cases with (c),(d) uniform wind and (a),(b) zero wind aloft.

Figure 7 shows $R^*_{\max}$ and the cold-pool propagation speed C as a function of U_s and U_∞. It is apparent that the rain rate increases with shear, from the upper-left to the lower-right side of Fig. 7a. For the present experimental study where the ambient wind comes from the left, the focus is on the cold pools that propagate toward the left (upstream) side of the channel (negative values of C; Fig. 7b); quasi-stationary solutions are simulated when the upwind cold-pool propagation is approximately countered by the environmental wind (expts B.2, B.8, B.10, and B.12 in Table 2). The cold pool propagates downstream only when both U_s and U_∞ are large in the region on the upper-right side of Fig. 7b. Figure 7b shows that the cold-pool propagation speed depends both on the wind speed at the ground and in the middle troposphere. These results are consistent with the previous studies mentioned above but note that at shears greater than $20\,\mathrm{m\,s^{-1}}/5\,\mathrm{km}$ (not done here), it is expected that $R^*_{\max}$ should decrease with further increases in shear [see Fig. 7 of Bryan et al. (2006)].

Focusing on the nearly stationary states in both sets of experiments (roughly in the area $15 < U_s < 20\,\mathrm{m\,s^{-1}}$, $0 < U_\infty < 15\,\mathrm{m\,s^{-1}}$), Fig. 7a shows that $R^*_{\max}$ generally increases for increasing shear, while in contrast, Fig. 4a indicates no change in $R_{\max}$ with shear until a threshold is crossed (near the thick dashed line). This differing behavior indicates that the increase in $R_{\max}$ with shear for the orographic case (Fig. 4a) is not a simple superposition of squall-line dynamics and orographic uplift. For example, in some no-mountain experiments showing a quasi-stationary solution (in which $R^*_{\max} \approx R_{\max}$),

TABLE 2. As in Table 1, but for no-mountain experiments (with $h_s = 5$ km and $Z_s = 0$), initialized with a cold potential temperature perturbation: $R^*_{\max}$ and R_{tot} calculated for all solutions (including nonstationary). The cold-pool propagation speed is given by C (calculated in the last 3 h of simulation).

Expt	U_s ($\mathrm{m\,s^{-1}}$)	U_∞ ($\mathrm{m\,s^{-1}}$)	R_{tot} ($10^3\,\mathrm{mm\,h^{-1}\,km^2}$)	$R^*_{\max}$ ($\mathrm{mm\,h^{-1}}$)	C ($\mathrm{m\,s^{-1}}$)
B.1	10	10	8	5	−5
B.2	15	15	7	4	1
B.3	20	20	7	4	8
B.4	10	5	12	14	−7
B.5	20	15	10	14	3
B.6	5	−5	11	10	−18
B.7	10	0	15	21	−6
B.8	17	7	11	29	−1
B.9	10	−5	12	19	−8
B.10	20	5	12	33	0
B.11	10	−10	14	26	−10
B.12	20	0	18	56	1

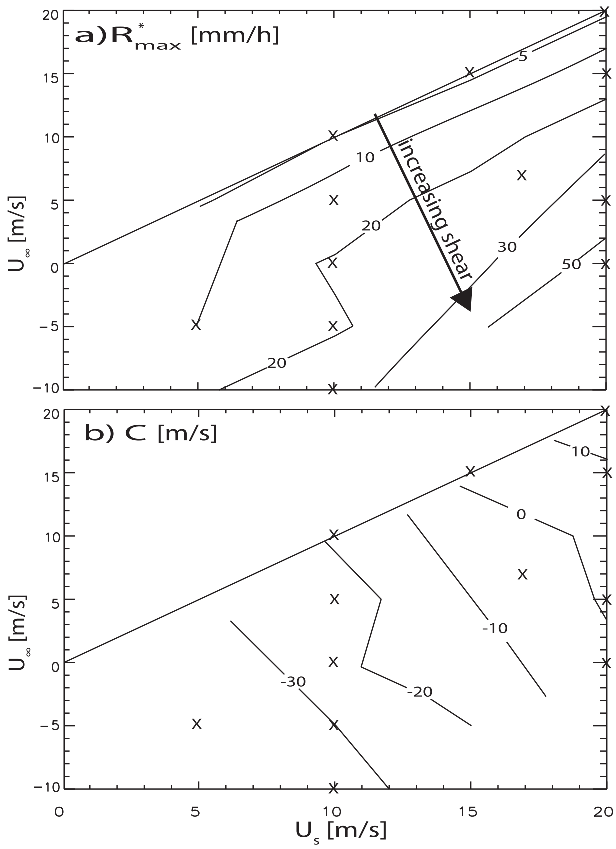

FIG. 7. (a) R^*_{max} from (4) (mm h^{-1}) and (b) C (m s^{-1}) as a function of U_s and U_∞ for experiments without the mountain; the crosses correspond to the experiments.

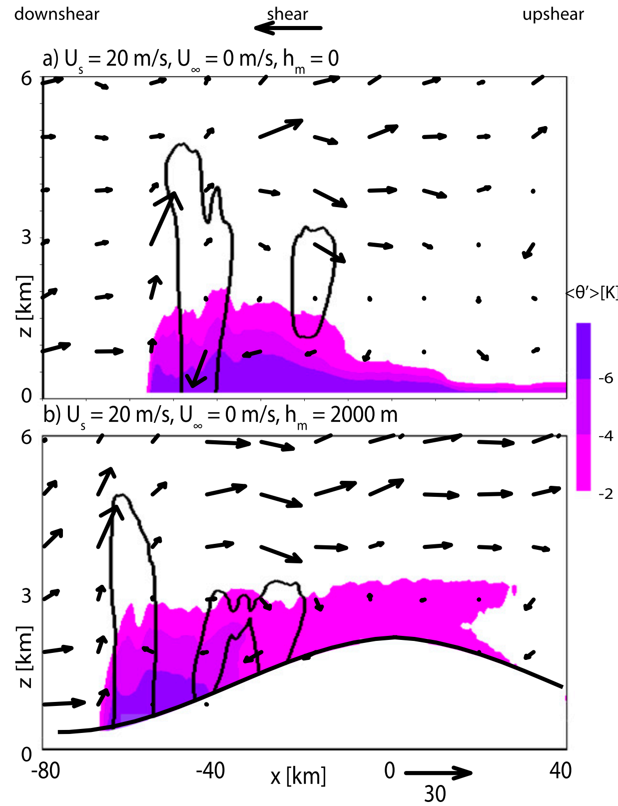

FIG. 8. Cross section of y average of potential temperature perturbation for (b) expt A.14 (U_s = 20 m s^{-1}, U_∞ = 0 m s^{-1}, h_m = 2000 m) and (a) expt B.12 (U_s = 20 m s^{-1}, U_∞ = 0 m s^{-1}, h_m = 0) after 10 h. Rainwater content contour line for 1.0 × 10^{-3} kg kg^{-1} is also shown.

R^*_{max} is much larger than in the corresponding case with the mountain (cf. expt B.12 versus expt A.14, and expt B.10 versus expt A.16). An explanation for this behavior is provided here in terms of cold-pool dynamics interacting with the mountain barrier.

Figure 8 shows the y-averaged potential temperature perturbation and rainwater content at t = 10 h for expts B.12 and A.14. It is apparent in Fig. 8a that, without the mountain, the upshear side of the cold pool propagates in a shallow layer, while its head is deeper on the downshear side, according to the mechanisms described in Rotunno et al. (1988). On the other hand, Fig. 8b shows that the presence of the mountain prevents the upshear side of the cold pool from propagating downwind, piling up the cooler air on the upstream side of the mountain. As a consequence, the density current with the mountain reaches a deeper depth as compared to the case without the mountain; the intensity of the potential temperature anomaly is comparable in the two cases (approximately −8 K).

The propagation of the density currents can be analyzed according to the theory discussed in Benjamin (1968) and Klemp et al. (1994). Considering the depth of the cold pool H as approximately equal to the height of the −4-K potential temperature anomaly, H is evaluated, respectively, as approximately 2 and 1.3 km in the two cases. Thus, since the cold-pool propagation speed is $C_s = \sqrt{2gH}$ (for an infinitely deep channel), where $g' = g(\theta_1 - \theta_0)/\theta_0$ is the reduced gravity (where θ_1 is the potential temperature of the environment and θ_0 that of the cold air), C_s is larger than the environmental wind (U_s = 20 m s^{-1}) in the case with the mountain, and the cold pool propagates upstream, producing an extensive region of increased wind speed above its head (Fig. 8b), which, in turn, advects the convective cells downstream, thus producing conditions less favorable to localized rainfall accumulations. On the other hand, in the cases without the mountain (Fig. 8a), the propagation speed of the cold pool is smaller because of its smaller depth and thus its propagation is approximately countered by the environmental wind—$(2g'H)^{1/2} \approx U_s$ = 20 m s^{-1}. This behavior can be interpreted in terms of the conceptual models developed in Weisman (1992): the situation for

TABLE 3. As in Table 1, but for experiments with different shear-layer depths h_s and bottom heights Z_s for $(U_s, U_\infty) = (20, 0)\,\mathrm{m\,s^{-1}}$, and a mountain with $h_m = 2000$ m and $a = 30$ km ($h_m/a = 0.07$; h_m/LFC = 1.11). Also experiments with uniform wind speed are included.

Expt	Z_s (km)	h_s (km)	R_{tot} (10^3 mm h^{-1} km^2)	R_{max} (mm h^{-1})	X_{max} (km)	τ_a/τ_c
C.1	0	2.5	25	NS	−120	23.1
A.14	0	5.0	28	30	−42	11.5
C.2	0	7.5	20	13	−10	8.7
C.3	0	10.0	18	14	−7	7.7
C.4	2.5	2.5	30	19	−7	7.7
C.5	2.5	5.0	20	15	−6	6.6
C.6	2.5	7.5	18	15	−1	6.3
C.7	5.0	5.0	18	17	1	5.8
	U_s	U_∞				
A.8	10	10.0	9	6	−5	11.5
A.18	20	20.0	15	16	−1	5.8

the case with the mountain is similar to his Fig. 2c, where the cold-pool circulation tilts the convective system upshear, while the no-mountain case can be compared to his Fig. 2b, where the circulation generated by the cold pool balances the ambient flow and the system becomes upright.

5. Additional experiments

To further explore the parameter space, additional experiments were performed changing the shear-layer parameters and the mountain shape.

a. *Changes in shear-layer extent and depth*

Table 3 shows the rainfall characteristics corresponding to different wind profiles for the case $(U_s, U_\infty) = (20, 0)\,\mathrm{m\,s^{-1}}$. It is apparent that the depth and the location of the shear layer can significantly influence the nature of the solution. When $Z_s = 0$, and the shear is confined to a very shallow layer ($h_s = 2.5$ km), the vertically averaged wind speed is not effective in maintaining the cold pool near the mountain; as a consequence, the cold pool propagates upstream (expt C.1).

As discussed in section 2, when the shear extends over a deeper layer ($h_s = 5$ km), an optimal balance is reached (expt A.14); the cold pool remains nearly stationary upstream of the mountain, favoring the rainfall accumulation in a limited area. A further extension of the shear depth, respectively, to 7.5 (expt C.2) and 10 km (expt C.3) has the effect of increasing the average ambient wind: thus, the cold pool is displaced downstream and the solutions are similar to the case with uniform wind speed (expt A.18). Compared to the no-shear expt A.18, Table 3 indicates that expts C.2 and C.3 show larger R_{tot} even though R_{max} is similar in all cases. This is a consequence of deeper convective cells in the cases with wind shear.

When the value of Z_s is increased (Table 3, expts C.4–C.7), all solutions show orographic precipitation (little or no enhancement of R_{max} with respect to the no-shear expt A.18) with a downstream-propagating cold pool. This finding is consistent with those of Weisman and Rotunno (2004) showing a weaker convective response to the shear layer when it is placed at levels above the cold pool (see their Fig. 18). However, in some cases of elevated shear, R_{tot} can be increased. For example, compared to expt A.14, in the experiment with $Z_s = 2.5$ km and $h_s = 2.5$ km (expt C.4) the intense low-level forcing combined with zero wind aloft produces deep convective cells extending over a wide area, favoring a large R_{tot}. For the other experiments with $Z_s = 2.5$ km and $Z_s = 5$ km (expts C.5–C.7), R_{max} and R_{tot} are similar to those of expts C.2 and C.3.

b. *Changes in mountain shape*

An additional set of experiments for the case $(U_s, U_\infty) = (20, 0)\,\mathrm{m\,s^{-1}}$ was performed by changing the mountain shape, both in terms of mountain height and half-width. Solutions are qualitatively similar in all cases, showing a quasi-stationary cold pool near the mountain. However, for the simulations with a higher ($h_m = 2$ km) or larger ($a = 50$ km) mountain, the cold pool propagates farther upstream, while for the cases with shorter and/or narrower mountains the cold pool remains confined near the mountain peak (see X_{max} in Table 4).

Differences of rainfall characteristics can also be observed in Table 4. With respect to R_{tot}, the variations among the experiments are relatively small, with slightly larger values for the simulations with higher and wider mountains. Differences in R_{max} are more significant: the rainfall peak increases for decreasing mountain heights, so that, for a fixed half-width, the R_{max} values are about 2 times larger for $h_m = 500$ m than for $h_m = 2000$ m. As discussed in section 3, these differences can be interpreted in terms of the effect of the orography and shear on cold-pool propagation. Figure 9a shows that for the highest mountain, the cold air piles up upwind, producing a deeper cold pool with a larger upwind propagation speed that is not countered by the environmental wind. As a consequence, the cold-pool propagates upstream and produces a front-to-rear flow that tilts the cells downstream and thereby decreases R_{max}. On the other hand, for lower mountains, the cold pool is shallower and is approximately balanced by the environmental wind. Thus, it remains stationary near the mountain peak, producing upright cells and larger R_{max} as in the no-mountain case (Weisman 1992). In other words, as h_m becomes smaller, the solution for the applied wind profile

TABLE 4. As in Table 1, but for experiments with different mountain shapes for $(U_s, U_\infty) = (20, 0)\,\mathrm{m\,s^{-1}}$, $Z_s = 0$, and $h_s = 5$ km.

Expt	h_m (km)	a (km)	R_{tot} (10^3 mm h^{-1} km^2)	R_{max} (mm h^{-1})	X_{max} (km)	τ_a/τ_c	h_m/a	h_m/LFC
A.14	2	30	28	30	−42	11.5	0.07	1.11
D.1	2	50	29	22	−60	19.2	0.04	1.11
D.2	1	15	26	31	−4	5.8	0.07	0.56
D.3	1	30	24	48	−4	11.5	0.03	0.56
D.4	1	50	25	29	−22	19.2	0.02	0.56
D.5	0.5	15	22	41	2	5.8	0.03	0.28
D.6	0.5	30	21	66	2	11.5	0.02	0.28
D.7	0.5	50	21	41	−10	19.2	0.01	0.28

approaches that of the no-mountain most intense squall line that is stationary at the mountain location.

An equally strong dependence of R_{max} is observed on a for a given h_m. The maximum rainfall peak is simulated for an optimal mountain half-width of $a = 30$ km, with smaller values reported for both narrower and wider mountains. To understand this behavior, the impact of nonlinear downwind advection by the enhanced high-terrain winds on the cold-pool propagation should also be considered. In particular, for wider ridges, associated with a weaker downslope wind, the density current can propagate against the flow; for narrower and steeper ridges, the downslope wind is strong enough to counterbalance the cold-pool propagation, so that it can remain quasi stationary near the mountain top ($a = 30$ km) or on the downstream side of the ridge ($a = 15$ km). In the latter case, the unfavorable location of the cold pool in the steep leeside works against larger values of R_{max}.

6. Discussion and conclusions

The present study extends the analysis started in MR12. That paper shows that, in some case studies, wind variations with height (including a low-level jet and zero wind aloft) need to be considered in numerical simulations of conditionally unstable flows past an idealized mesoscale mountain ridge in order to obtain larger rainfall rates that are in closer agreement with observations. Here, the effect of the wind profile on the solution is analyzed in a systematic way, by performing numerical experiments using the Weisman–Klemp sounding but including vertical wind shear.

By exploring the parameter space identified by the surface and the upper-level wind speeds, two main categories of solutions are identified, characterized, respectively, by stationary orographic rainfall and nonstationary, upstream-propagating cold pools. The principal features of the solutions are mainly the result of a delicate balance between the propagation of the cold pool (produced by the evaporative cooling of rain from precipitating convective clouds) away from the mountain and the advection by the environmental wind toward it.

Without wind shear, MR09 found that, when the wind speed is strong enough, there is not enough time for the cold pool to develop through evaporation of rain into midlevel air; when the vertically averaged wind speed is too weak, it cannot prevent the cold pool, formed near

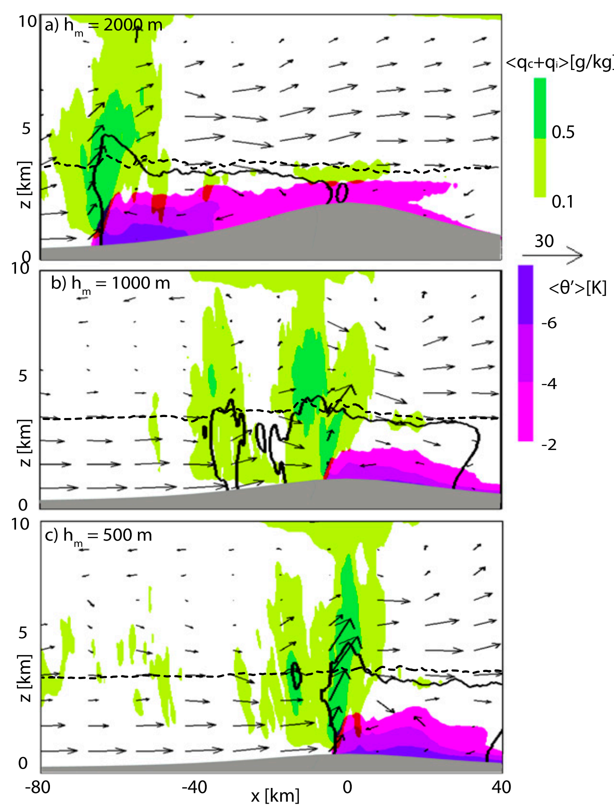

FIG. 9. Vertical cross section of the y average of potential temperature perturbation (purple shaded areas), cloud water plus ice content (green shaded areas), rainwater content (solid contour line for 0.5×10^{-3} kg kg^{-1}), wind vectors (arrows), and 0°C isotherm (dashed line). The results are shown for experiments with $U_s = 20\,\mathrm{m\,s^{-1}}$, $U_\infty = 0\,\mathrm{m\,s^{-1}}$, and different mountain heights [(a) expt A.14, $h_m = 2000$ m; (b) expt D.3, $h_m = 1000$ m; (c) expt D.6, $h_m = 500$ m). The vertical cross sections are shown at the final integration time $t = 10$ h.

the mountain, from propagating far upstream from the obstacle. In both cases, according to Rotunno–Klemp–Weisman (RKW) theory (Rotunno et al. 1988), the cold-pool-triggered updrafts are shallow and not favorable for large rainfall production and accumulation. The inclusion of wind shear changes both the propagation speed of the cold pool and the ability to produce deep convective cells (as described in RKW). For certain optimal combinations of the surface wind and the wind aloft, a quasi-stationary cold pool, with intense convective cells near the mountain ridge, produces the greatest rain rates and total rainfalls. An additional important aspect of the optimal solution is that, as the cells grow into upper layers characterized by very weak wind, they are no longer advected with respect to the mountain, and produce a more stationary rainfall pattern. A cold pool remaining quasi stationary on the upwind slope is the most favorable condition in terms of rainfall accumulation, since it behaves as an extension of the orographic obstacle and thus may enhance the orographic uplift.

Comparison of sheared-environment simulations with and without orography indicates that the mountain can have a significant effect on the cold pool, and, therefore, a simple superposition of cold-pool and orographic-flow effects does not explain the dependence of rain rate on shear in the present experiments. To get the intense rainfall rates, a nearly exact balance between the ground-relative speed of the cold pool and the near-surface environmental wind is needed; however, this balance depends on how the mountain affects the cold pool. For example, the present solutions indicate that the orography can act as a barrier that piles up cold air on its upwind side and produces deeper cold pools than would otherwise occur for the same sounding. These deeper cold pools induce faster ground-relative cold-pool propagation speeds than would otherwise be obtained. Similar considerations can be used to explain the sensitivity of the solutions to the shear-layer depth and to the mountain shape.

Since real-world episodes of heavy orographic convection are very complex (e.g., because of the three dimensionality of the flow and of the topography and the time evolution of the synoptic situation), the extremely simplified setup used here, with very idealized atmospheric profiles and topography, cannot be applied to interpret realistic case studies. Rather, the present study shows the positive effect of vertical wind shear on the orographic rainfall accumulation, at least for the reverse-shear profiles considered here, confirming the outcomes of MR12. In particular, the present simulations show that a low-level cross-mountain flow combined with zero wind aloft is important for the generation of intense rainfall not only as a moisture-transport and convection-focusing mechanism but, also for producing deeper and stronger convective cells.

Considering the additional simulations performed here, it is interesting to look for an extension of the functional relation for precipitation identified in MR09 and MR10, including additional nondimensional numbers related to vertical wind shear (see Fig. 1). Since two additional length scales are introduced (Z_s and h_s), and two wind speeds (U_s and U_∞) are in place of U, three additional nondimensional numbers should be included. It is beyond the scope of the present study to identify such nontrivial functional dependences. However, the substitution in τ_a/τ_c of U with the average of wind speed in the lower 5 km (which, in most cases, is equal to the average of U_s and U_∞) is found to be able to represent the gross behavior of the solutions in most of the simulations (see Tables 1, 2, and 4) in the framework of MR09 theory. In particular, a large value of this parameter ($\tau_a/\tau_c > 15$) generally corresponds to the presence of nonstationary cold pools, while values of $\tau_a/\tau_c \sim 10$ correspond to solutions with stationary rainfall near the mountain, modulated by the values of the other two parameters (h_m/a and h_m/LFC; see Fig. 1 in MR12).

A limitation of the present analysis is that only the wind component perpendicular to the ridge u is considered here. However, the along-ridge component v is often the only one observed in the upper troposphere in orographic convective heavy-rain events. Just to mention a few cases, an intense low-level jet and a weak upper-level along-ridge component were identified upstream in the Big Thompson storm [Fig. 5b in Caracena et al. (1979)], the Oahu flood [wind profiles at 0200 UTC 19 April 1974 in Fig. 5 of Schroeder (1977)], and the Vaison-La-Romaine flash flood [Fig. 6a in Senesi et al. (1996)] and were noted to be common ingredients in several terrain-induced convective flooding events [Fig. 24 in Pontrelli et al. (1999)]. Compared to experiments initialized only with the u component, the presence of a $v(z)$ (a constant v should produce no effect given the two-dimensional mountain ridge used here) could modify the cell structure and somewhat modify the solutions. To analyze the sensitivity of the solution to the along-ridge component of wind shear, a couple of additional simulations have been performed repeating expts A.3 and A.14, but including a v component in the initial profile with a shear of the same intensity as u but reversed ($v = 0$ at the ground and respectively $v = 10$ or $20\,\mathrm{m\,s^{-1}}$ above 5 km). Simulations show that the inclusion of $v(z)$ does not change the structure of the solutions and the intensity of the rainfall. This result suggests that, in the absence of along-ridge flow variations, the upper-level along-ridge component of the shear does not produce major changes. However, the generality of this result should be tested in a larger set of experiments, using domains larger than those employed here; this is left for a future study.

Several convective episodes related to the interaction of the flow with the orography occurred during the first special observing period (SOP1) campaign in the framework of the Hydrological cycle in the Mediterranean Experiment (HyMeX; http://www.hymex.org), an international program aiming at advancing the scientific knowledge of the water cycle in the Mediterranean. In particular, SOP1 took place over the western Mediterranean during fall 2012 and focused on heavy precipitation and flash flood events. Several intensive observation periods (IOPs) were analyzed with a plethora of different models running in real time and with an extraordinary deployment of advanced instrumentation. UHF profilers, radiosondes, and dropsondes reported on vertical profiles similar to those discussed in the present study (see ''IOP overview summary'' in http://sop.hymex.org/). A deeper analysis of such events will enrich our knowledge of conditionally unstable flows over orography and in particular will shed more light on aspects related to the genesis and evolution of convective cells.

Acknowledgments. The stay of M. M. Miglietta in Boulder was supported by NCAR. Comments by George Bryan and Morris Weisman and three anonymous reviewers on the first draft of this paper are gratefully acknowledged.

REFERENCES

Benjamin, T. B., 1968: Gravity currents and related phenomena. *J. Fluid Mech.,* **31,** 209–248, doi:10.1017/S0022112068000133.

Bousquet, O., and B. F. Smull, 2003: Airflow and precipitation fields within deep alpine valleys observed by airborne Doppler radar. *J. Appl. Meteor.,* **42,** 1497–1513, doi:10.1175/1520-0450(2003)042<1497:AAPFWD>2.0.CO;2.

Bryan, G. H., and J. M. Fritsch, 2002: A benchmark simulation for moist nonhydrostatic models. *Mon. Wea. Rev.,* **130,** 2917–2928, doi:10.1175/1520-0493(2002)130<2917:ABSFMN>2.0.CO;2.

——, J. C. Wyngaard, and J. M. Fritsch, 2003: Resolution requirements for the simulation of deep moist convection. *Mon. Wea. Rev.,* **131,** 2394–2415, doi:10.1175/1520-0493(2003)131<2394:RRFTSO>2.0.CO;2.

——, J. C. Knievel, and M. D. Parker, 2006: A multimodel assessment of RKW theory's relevance to squall-line characteristics. *Mon. Wea. Rev.,* **134,** 2772–2792, doi:10.1175/MWR3226.1.

Buzzi, A., and L. Foschini, 2000: Mesoscale meteorological features associated with heavy precipitation in the southern Alpine region. *Meteor. Atmos. Phys.,* **72,** 131–146, doi:10.1007/s007030050011.

Caracena, F. R., A. Maddox, L. R. Hoxit, and C. F. Chappell, 1979: Meso-analysis of the Big Thompson storm. *Mon. Wea. Rev.,* **107,** 1–17, doi:10.1175/1520-0493(1979)107<0001:MOTBTS>2.0.CO;2.

Davis, C. A., and W.-C. Lee, 2012: Mesoscale analysis of heavy rainfall episodes from SoWMEX/TiMREX. *J. Atmos. Sci.,* **69,** 521–537, doi:10.1175/JAS-D-11-0120.1.

Davolio, S., A. Buzzi, and P. Malguzzi, 2009: Orographic triggering of long-lived convection in three dimensions. *Meteor. Atmos. Phys.,* **103,** 35–44, doi:10.1007/s00703-008-0332-5.

Ducrocq, V., O. Nuissier, D. Ricard, C. Lebeaupin, and T. Thouvenin, 2008: A numerical study of three catastrophic precipitating events over western Mediterranean region (southern France). Part II: Mesoscale triggering and stationarity factors. *Quart. J. Roy. Meteor. Soc.,* **134,** 131–145, doi:10.1002/qj.199.

Fovell, R. G., 1991: Influence of the Coriolis force on two-dimensional model storms. *Mon. Wea. Rev.,* **119,** 606–630, doi:10.1175/1520-0493(1991)119<0606:IOTCFO>2.0.CO;2.

Fuhrer, O., and C. Schär, 2005: Embedded cellular convection in moist flow past topography. *J. Atmos. Sci.,* **62,** 2810–2828, doi:10.1175/JAS3512.1.

——, and ——, 2007: Dynamics of orographically triggered banded convection in sheared moist orographic flows. *J. Atmos. Sci.,* **64,** 3542–3561, doi:10.1175/JAS4024.1.

Houze, R. A., Jr., and S. Medina, 2005: Turbulence as a mechanism for orographic precipitation enhancement. *J. Atmos. Sci.,* **62,** 3599–3623, doi:10.1175/JAS3555.1.

Kirshbaum, D. J., and D. R. Durran, 2005a: Atmospheric factors governing banded orographic convection. *J. Atmos. Sci.,* **62,** 3758–3774, doi:10.1175/JAS3568.1.

——, and ——, 2005b: Observations and modeling of banded orographic convection. *J. Atmos. Sci.,* **62,** 1463–1479, doi:10.1175/JAS3417.1.

Klemp, J. B., and D. K. Lilly, 1975: The dynamics of wave-induced downslope winds. *J. Atmos. Sci.,* **32,** 320–339, doi:10.1175/1520-0469(1975)032<0320:TDOWID>2.0.CO;2.

——, R. Rotunno, and W. C. Skamarock, 1994: On the dynamics of gravity currents in a channel. *J. Fluid Mech.,* **269,** 169–198, doi:10.1017/S0022112094001527.

Kodama, K., and G. M. Barnes, 1997: Heavy rain events over the south-facing slopes of Hawaii: Attendant conditions. *Wea. Forecasting,* **12,** 347–367, doi:10.1175/1520-0434(1997)012<0347:HREOTS>2.0.CO;2.

Lin, Y.-L., S. Chao, T.-A. Wang, M. L. Kaplan, and R. P. Weglarz, 2001: Some common ingredients for heavy orographic rainfall. *Wea. Forecasting,* **16,** 633–660, doi:10.1175/1520-0434(2001)016<0633:SCIFHO>2.0.CO;2.

Miglietta, M. M., and R. Rotunno, 2009: Numerical simulations of conditionally unstable flows over a ridge. *J. Atmos. Sci.,* **66,** 1865–1885, doi:10.1175/2009JAS2902.1.

——, and ——, 2010: Numerical simulations of low-CAPE flows over a mountain ridge. *J. Atmos. Sci.,* **67,** 2391–2401, doi:10.1175/2010JAS3378.1.

——, and ——, 2012: Application of theory to observed cases of orographically forced convective rainfall. *Mon. Wea. Rev.,* **140,** 3039–3053, doi:10.1175/MWR-D-11-00253.1.

Miniscloux, F., J. D. Creutin, and S. Anquetin, 2001: Geostatistical analysis of orographic rainbands. *J. Appl. Meteor.,* **40,** 1835–1854, doi:10.1175/1520-0450(2001)040<1835:GAOOR>2.0.CO;2.

Neiman, P. J., G. A. Wick, F. M. Ralph, B. E. Martner, A. B. White, and D. E. Kingsmill, 2005: Wintertime nonbrightband rain in California and Oregon during CALJET and PACJET: Geographic, interannual, and synoptic variability. *Mon. Wea. Rev.,* **133,** 1199–1223, doi:10.1175/MWR2919.1.

Nuissier, O., V. Ducrocq, D. Ricard, C. Lebeaupin, and S. Anquetin, 2008: A numerical study of three catastrophic precipitating events over southern France. I: Numerical framework and synoptic ingredients. *Quart. J. Roy. Meteor. Soc.,* **134,** 111–130, doi:10.1002/qj.200.

Pontrelli, M. D., G. H. Bryan, and J. M. Fritsch, 1999: The Madison County, Virginia, flash flood of 27 June 1995. *Wea. Forecasting,* **14,** 384–404, doi:10.1175/1520-0434(1999)014<0384:TMCVFF>2.0.CO;2.

Richard, E., A. Buzzi, and G. Zängl, 2007: Quantitative precipitation forecasting in the Alps: The advances achieved by the Mesoscale Alpine Programme. *Quart. J. Roy. Meteor. Soc.,* **133,** 831–846, doi:10.1002/qj.65.

Romero, R., C. A. Doswell III, and C. Ramis, 2000: Mesoscale numerical study of two cases of long-lived quasi-stationary convective systems over eastern Spain. *Mon. Wea. Rev.,* **128,** 3731–3751, doi:10.1175/1520-0493(2001)129<3731:MNSOTC>2.0.CO;2.

Rotach, M. W., and Coauthors, 2009: MAP D-PHASE: Real-time demonstration of weather forecast quality in the alpine region. *Bull. Amer. Meteor. Soc.,* **90,** 1321–1336, doi:10.1175/2009BAMS2776.1.

Rotunno, R., and R. A. Houze, 2007: Lessons on orographic precipitation from the Mesoscale Alpine Programme. *Quart. J. Roy. Meteor. Soc.,* **133,** 811–830, doi:10.1002/qj.67.

——, J. B. Klemp, and M. L. Weisman, 1988: A theory for strong, long-lived squall lines. *J. Atmos. Sci.,* **45,** 463–485, doi:10.1175/1520-0469(1988)045<0463:ATFSLL>2.0.CO;2.

Sawyer, J. S., 1956: The physical and dynamical problems of orographic rain. *Weather,* **11,** 375–381, doi:10.1002/j.1477-8696.1956.tb00264.x.

Schroeder, T. A., 1977: Meteorological analysis of an Oahu flood. *Mon. Wea. Rev.,* **105,** 458–468, doi:10.1175/1520-0493(1977)105<0458:MAOAOF>2.0.CO;2.

Senesi, S., P. Bougeault, J.-L. Chèze, P. Cosentino, and R.-M. Thepenier, 1996: The Vaison-La-Romaine flash flood: Mesoscale analysis and predictability issues. *Wea. Forecasting,* **11,** 417–442, doi:10.1175/1520-0434(1996)011<0417:TVLRFF>2.0.CO;2.

Smith, R. B., 1979: The influence of mountains on the atmosphere. *Advances in Geophysics,* Vol. 21, Academic Press, 87–230.

Szeto, K. K., and H.-R. Cho, 1994: A numerical investigation of squall lines. Part III. Sensitivity to precipitation processes and the Coriolis force. *J. Atmos. Sci.,* **51,** 1341–1351, doi:10.1175/1520-0469(1994)051<1341:ANIOSL>2.0.CO;2.

Weisman, M. L., 1992: The role of convectively generated rear-inflow jets in the evolution of long-lived mesoconvective systems. *J. Atmos. Sci.,* **49,** 1826–1847, doi:10.1175/1520-0469(1992)049<1826:TROCGR>2.0.CO;2.

——, and J. B. Klemp, 1982: The dependence of numerically simulated convective storms on vertical wind shear and buoyancy. *Mon. Wea. Rev.,* **110,** 504–520, doi:10.1175/1520-0493(1982)110<0504:TDONSC>2.0.CO;2.

——, and R. Rotunno, 2004: "A theory for strong long-lived squall lines" revisited. *J. Atmos. Sci.,* **61,** 361–382, doi:10.1175/1520-0469(2004)061<0361:ATFSLS>2.0.CO;2.

Wulfmeyer, V., and Coauthors, 2011: The Convective and Orographically-induced Precipitation Study (COPS): The scientific strategy, the field phase, and research highlights. *Quart. J. Roy. Meteor. Soc.,* **137,** 3–30, doi:10.1002/qj.752.

Yoshizaki, M., and Y. Ogura, 1988: Two- and three-dimensional modelling studies of the Big Thompson storm. *J. Atmos. Sci.,* **45,** 3700–3722, doi:10.1175/1520-0469(1988)045<3700:TATDMS>2.0.CO;2.

——, T. Kato, Y. Tanaka, H. Takayama, Y. Shoji, H. Seko, K. Arao, and K. Manabe, 2000: Analytical and numerical study of the 26 June 1998 orographic rainband observed in western Kyushu, Japan. *J. Meteor. Soc. Japan,* **78,** 835–856.